Surfaces and Interfaces 48 (2024) 104316

Contents lists available at ScienceDirect

Surfaces and Interfaces

journal homepage: www.sciencedirect.com/journal/surfaces-and-interfaces

Structures, electronic properties, and delithiation thermodynamics of the heteroepitaxial α-Al_2O_3//$LiMn_2O_4$ (001) and (111) interfaces

Brian Ramogayana [a,b], David Santos-Carballal [b,*], Khomotso P. Maenetja [a], Phuti E. Ngoepe [a], Nora H. de Leeuw [b,c,*]

[a] Materials Modelling Centre, School of Physical and Mineral Sciences, University of Limpopo, Private Bag x1106, Sovenga 0727, South Africa
[b] School of Chemistry, University of Leeds, Leeds LS2 9JT, United Kingdom
[c] Department of Earth Sciences, Utrecht University, Princetonlaan 8a, 3584 CB Utrecht, The Netherlands

ARTICLE INFO

Keywords:
Heteroepitaxial interfaces
Aluminium oxide coating
Spinel surfaces
Li-ion batteries
DFT

ABSTRACT

Surface coatings play a pivotal role in enhancing the performance of secondary lithium-ion batteries by mitigating undesirable electrolyte activity towards the cathode materials. Metal oxide candidates have been investigated extensively, with α-Al_2O_3 emerging as a particularly promising coating material owing to its exceptional mechanical and thermal stability alongside low electrical conductivity. Despite the extensive exploration of this application of α-Al_2O_3, insight into the interplay between the coating layer and the cathode substrate remains incomplete. To address this lack of knowledge, this study employs density functional theory calculations with a Hubbard Hamiltonian and long-range dispersion corrections (DFT+*U*-D3) to comprehensively investigate the interfacial geometries, stabilities, and electronic properties of α-Al_2O_3-coated $LiMn_2O_4$ (001) and (111) interfaces of varying thicknesses. The individual surfaces were modelled first before constructing the interfaces. We found that the α-Al_2O_3 $(11\bar{2}0)$ and (0001) surfaces match the $LiMn_2O_4$ (001) and (111) facets well, exhibiting {1132} and {3121} configurations, respectively, with corresponding misfits of 2.40 and 2.75 %. We calculated the largest adhesion energies of 0.16 and 0.10 eV/Å^2 for monolayers with the {1132} and {3121} configurations, respectively, with the stability decreasing as the thickness of the α-Al_2O_3 layer increases. Further analysis reveals a minor charge accumulation on the substrate, attributed to charge accumulation on the oxygen atoms that participate in the Al-O bond. In contrast, we observed a depletion of charge on the manganese atoms that form the MnO_6 units. The vacancy formation energies increase following partial delithiation, prompting minor charge depletion on neighbouring Mn atoms in the form of charge redistribution. The calculated work function increases with respect to the pristine surfaces, indicating that the coated interfaces are less reactive.

1. Introduction

Lithium-ion batteries (LIBs) have led to remarkable advancements in everyday applications, and continue to evolve in terms of safety, capacity, power, cycling stability and energy density since their commercialization was started by Sony in 1991 [1]. This impressive progress has been attributed to the integration of novel and tailored active (cathode) materials possessing larger capacity, enhanced potential and improved thermal stability [2–4]. An early example of cathode material innovation was the development of lithium cobalt oxide ($LiCoO_2$) with a layered rhombohedral structure ($R\bar{3}m$), initially proposed by Mizushima et al. [5] in 1980. Despite the noteworthy theoretical capacity of $LiCoO_2$ of 274 mAh/g, practical applications are constrained by a charging voltage limit of 4.45 V, yielding merely ~170 mAh/g (less than 50 % of its theoretical capacity) [6]. The material's capacity fades after 10 cycles, primarily due to (*i*) structural phase transitions followed by lattice deformations, engendering particle strain and crack formation and (*ii*) surface-electrolyte interactions resulting in Co dissolution and oxygen depletion from the surface. Additionally, cobalt usage entails environmental concerns and substantial costs [7].

Various alternatives to $LiCoO_2$ as cathode materials have been explored and categorized structurally into three groups: layered [8–10], spinels [11,12], and olivines [13–15]. The spinel material $LiMn_2O_4$ as introduced by Thackeray et al. in 1983 [16] is often considered an effective substitute for $LiCoO_2$ due to its manganese content, which is abundant, less toxic, and cost-effective. Structurally, $LiMn_2O_4$ consists of

* Corresponding authors.
E-mail addresses: D.Santos-Carballal@leeds.ac.uk (D. Santos-Carballal), n.h.deleeuw@leeds.ac.uk (N.H. de Leeuw).

https://doi.org/10.1016/j.surfin.2024.104316
Received 18 December 2023; Received in revised form 29 March 2024; Accepted 7 April 2024
Available online 10 April 2024
2468-0230/© 2024 The Author(s). Published by Elsevier B.V. This is an open access article under the CC BY license (http://creativecommons.org/licenses/by/4.0/).

a three-dimensional framework with diffusion pathways that facilitate unhindered Li^+ transport, retaining the integrity of the parent Mn_2O_4 material during full delithiation [17,18]. However, when used as a cathode material, $LiMn_2O_4$ suffers from capacity fading due to electrolyte activity, which induces Jahn-Teller distortion of the Mn^{3+} ions [19–21], cathode-electrolyte interphase (CEI) formation [22,23], and dissolution of Mn^{2+} ions into the electrolyte [24–26]. To overcome these issues, remedies such as the introduction of protective coating materials [27–29], cation/anion doping [30,31,27], and enhancing the proportion of the $LiMn_2O_4$ (111) surface in the morphology [32–34] have been pursued. Among these, surface coating has emerged as a strong strategy to hinder electrolyte-cathode interactions while preserving the $LiMn_2O_4$ structural integrity. Various coating materials have been explored, including metallic oxides (*e.g.* TiO_2 [35,36], Al_2O_3 [37,38], ZnO [39–41], MgO [42,43]), fluorides (such as AlF_3 [44,45], SrF_2 [46] and LaF_3 [47]), and phosphates ($LaPO_4$ [48,49]), YPO_4 [50], $FePO_4$ [51], $AlPO_4$ [52]). α-Al_2O_3 stands out as a promising candidate due to its exceptional mechanical and thermal stability, corrosion resistance, and low electrical conductivity [53,54]. A notable feature is its ability to react with the acidic electrolyte medium, hydrofluoric acid (HF), resulting in the formation of an additional coating layer AlF_3 layer via the chemical equation: $Al_2O_3(s) + 6HF(aq) \rightarrow 2AlF_3(s) + 3H_2O(l)$, which further hinders electrolyte-cathode interactions [55].

Surface modification of $LiMn_2O_4$ via α-Al_2O_3, as demonstrated by Kanna and Manthirram [56] and Eftekari [57], offers enhanced long-term cyclability, sustained structural integrity, crystallinity during cycling, and improved capacity retention even at elevated temperatures. Tu et al. [58] achieved a nano-Al_2O_3-coated $LiMn_2O_4$ material through a melting-impregnation method, resulting in superior capacity retention at room temperature with a fading rate of only 0.037 % per cycle over 100 cycles. Al atom incorporation in the surface of the spinel was confirmed through X-ray absorption fine structure (XAFS). Employing density functional theory calculations, Ouyang et al. [59] elucidated that the presence of the Al_2O_3 coating restores the bonding of the under-coordinated octahedral manganese with oxygen at the (001) surface $LiMn_2O_4$.

In general, a good coating material should be thin, electrochemically stable, cost-effective, easy to synthesise, and display high ionic and electronic conductivity, as discussed by Nisar et al. [60]. Gaun et al. [61] reported improved electrochemical performance, suggesting that 10 atomic layer deposition (ALD) cycles yielded better cycling compared to 20 ALD cycles, due to the larger polarization and resistance resulting from increased coating thickness. Waller et al. [62] observed enhanced capacity retention and capability, along with the formation of Al-F bonds during cycling and the presence of Mn in the coating layers. Similar findings have been reported by Lai et al. [63] for $LiMn_2O_4$ enveloped by Al_2O_3 nanosheets. Warburton et al. [64–66] have employed calculations based on the density functional theory (DFT) to investigate theoretical aspects of the Al_2O_3 ALD mechanism on $LiMn_2O_4$ surfaces, in particular how the near-surface manganese oxidation evolves with different Al precursor ligands and the consequences for electrochemical performance [38] in comparison with experimental observations. However, pertinent *ab initio* studies exploring interfacial interactions and stability during cycling remain limited. As such, this study reports the results of DFT calculations of the heteroepitaxial interface stability of α-Al_2O_3-coated $LiMn_2O_4$ (001) and (111) surfaces with distinct coating thicknesses throughout cycling.

2. Simulation methods

Spin-polarized density functional theory calculations, as implemented in the Vienna *Ab-initio* Simulation Package (VASP), [67] have been employed to simulate the pristine and partially-delithiated α-Al_2O_3/$LiMn_2O_4$ heterostructures. The exchange-correlation energy was described using the Perdew, Burke, and Ernzerhof (PBE) functional within the generalized gradient approximation (GGA) [68]. A kinetic energy cut-off of 560 eV was applied for the expansion of the Kohn-Sham (KS) valence states. Γ-centred Monkhorst-Pack meshes of $5 \times 5 \times 5$ and $9 \times 9 \times 5$ *k*-points were used for the bulk structures of $LiMn_2O_4$ and Al_2O_3, respectively. The $LiMn_2O_4$ and α-Al_2O_3 surfaces, as well as the α-Al_2O_3//$LiMn_2O_4$ interfaces were modelled using $5 \times 5 \times 1$ and $1 \times 1 \times 1$ *k*-points grids, respectively. The projected augmented wave (PAW) formalism [69] as formulated by Kresse and Joubert [70] was employed to treat Li: $2s^1$, Mn: $3d^5 4s^2$, O: $2s^2 2p^4$ and Al: $3s^2 3p^1$ as valence electrons and their interaction with the core electrons. The semi-empirical method of Grimme with Becke-Johnson damping [D3-(BJ)] [71,72] was included to account for the long-range dispersion interactions. The tetrahedron method with Blöchl corrections was used to obtain accurate total energies and electronic properties [73]. To improve the convergence of the Brillouin zone integrations, a Gaussian smearing technique with a width of 0.05 eV was applied to all geometry optimizations [72]. A Hubbard correction [74] based on the formulation of Dudarev and co-workers [75] was introduced to improve the description of the localized 3*d* manganese electrons, where we have applied the effective parameter $U_{\text{eff}} = 4.0$ eV following the literature [76,77] and our previous studies [78,79]. Dipole corrections were applied in the direction perpendicular to the surface plane to improve the convergence of the electronic energy. Structural convergence was achieved using the conjugate-gradient technique and the convergence criterion was deemed met when the Hellmann–Feynman forces fell below 0.01 eV/Å.

3. Results and discussions

3.1. Bulk α-Al_2O_3 and $LiMn_2O_4$ phases

An ideal coating material for the cathode of Li-ion batteries should primarily be an insulator capable of forming a robust physical barrier with high thermal and ion conductivity. Moreover, it should exhibit non-reactivity towards the cathode surfaces, while offering protection against corrosive agents such as hydrofluoric acid (HF). Among the array of potential choices, corundum α-Al_2O_3 stands out, due to its remarkable mechanical and thermal stability, exceptional corrosion resistance, and its propensity to react with hydrofluoric acid (HF) to generate AlF_3, which possesses promising coating attributes [80]. The simulated α-Al_2O_3 material has hexagonal bulk crystal symmetry within the *R*3*c* (No. 167) space group. The unit cell is composed of 30 atoms: 12 aluminium atoms occupying two-thirds of the octahedral 12*c* Wyckoff positions with coordinate (0.000, 0.000, 0.148) and 18 oxygen atoms filling the 18*e* Wyckoff sites with the coordinate (0.306, 0.000, 0.250), which are aligned along the [001] direction. After optimization, the lattice parameters of the α-Al_2O_3 bulk structure are $a = b = 4.776$ Å and $c = 13.026$ Å, in agreement with reported experimental data [81–83] where $a = b = 4.751$ Å and $c = 12.868$ Å with deviations of ~0.52 and 1.22 % for *a* and *b*, respectively. Our calculations indicate average atomic charges within the α-Al_2O_3 bulk of $q(\text{Al}) = 2.48\ e^-$/atom and $q(\text{O}) = -1.65\ e^-$/atom. Corundum α-Al_2O_3, which is an electrical insulator, has a wide band gap of 5.91 eV in its calculated density of states, in agreement to within 1.02 % with the experimental value of 5.97 eV. [84] The valence band of α-Al_2O_3 is primarily influenced by oxygen 2*p* orbitals, accompanied by minor contributions from Al *s*, Al *p* and O *s* orbitals spanning the range of −6.93 to 0.12 eV. In contrast, the unoccupied conduction band spans from 0 to 6.10 eV, see Fig. 1a.

For the substrate cathode material, we considered the normal $LiMn_2O_4$ structure which crystallizes in a cubic structure with space group $Fd\bar{3}m$ (No. 227). Despite $LiMn_2O_4$ exhibiting partial inversion of approximately 30 % [82], here we have decided to use the fully normal spinel where the Li cations fill the tetrahedral positions, and the Mn atoms occupy the octahedral holes. Considering the partial inversion degree in the conventional cubic cell of a spinel material containing 56 atoms would entail simulating 4222 inequivalent configurations before creating the surface and interface models, which is outside the scope of

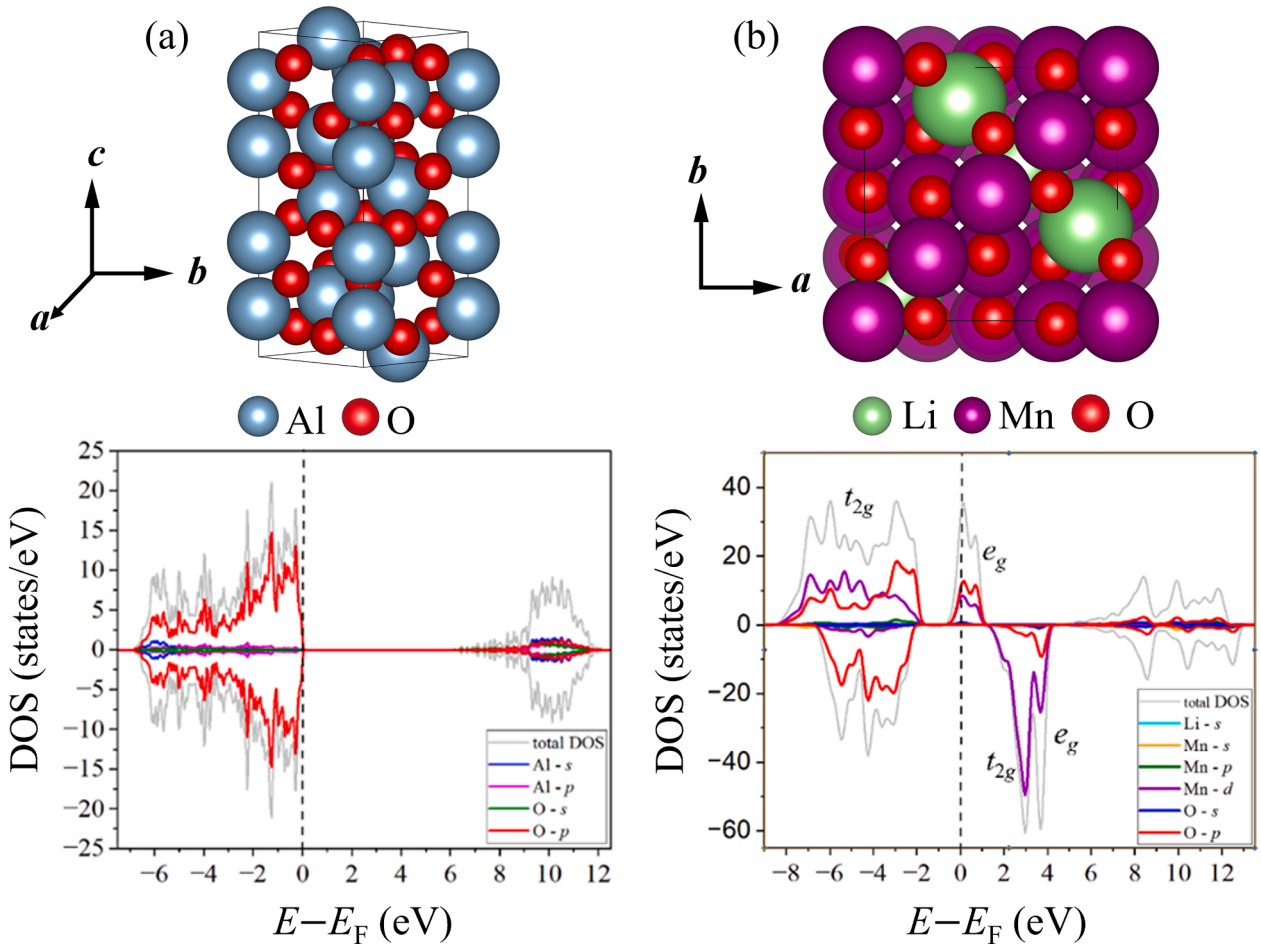

Fig. 1. (Left panels) Optimized crystal structures and (right panels) corresponding projected density of states (PDOS) of (a) $LiMn_2O_4$ and (b) α-Al_2O_3.

this work. In previous work, we have also successfully employed the (001), (011) and (111) surface models of the normal $LiMn_2O_4$ spinel to calculate their adsorption properties towards ethylene carbonate and hydrogen fluoride [76,83], and we are therefore confident that the normal spinel model will provide the insight into the interfacial structures and properties that are the subject of the current work.

The structure consists of a conventional unit cell comprising 56 atoms, wherein 8 Li ions occupy the 8*a* tetrahedral Wyckoff sites, 16 Mn cations are distributed across the 16*d* octahedral Wyckoff positions with an equal proportion of formally Mn^{3+} and Mn^{4+} ions averaging a charge of +3.5. Accompanying these are 32 O atoms located in a close-packed cubic array at the 32*e* Wyckoff sites, forming a face-centred cubic crystal lattice. The optimised lattice parameters $a = b = c = 8.347$ Å are in line with reported experimental data [30,85] of $a = 8.249$ Å, within ~1.18%, see Fig. 2a. The calculated average Mn-O bond distance measures ~1.989 Å for both Mn^{3+} and Mn^{4+}, in agreement with reported experimental values of 1.961 Å and close to another theoretical value of 1.867 Å [21]. The calculated density of states, previously discussed in [86,21], shows half-metallic behaviour with the Fermi level intersecting the spin-up e_g manganese (Mn^{3+}) ions and oxygen 2*p* orbitals, see Fig. 1b. The occupied valence band lies within the range of −8.5 to 2.3 eV, consisting of hybridized Mn t_{2g} states with O 2*p* orbitals,

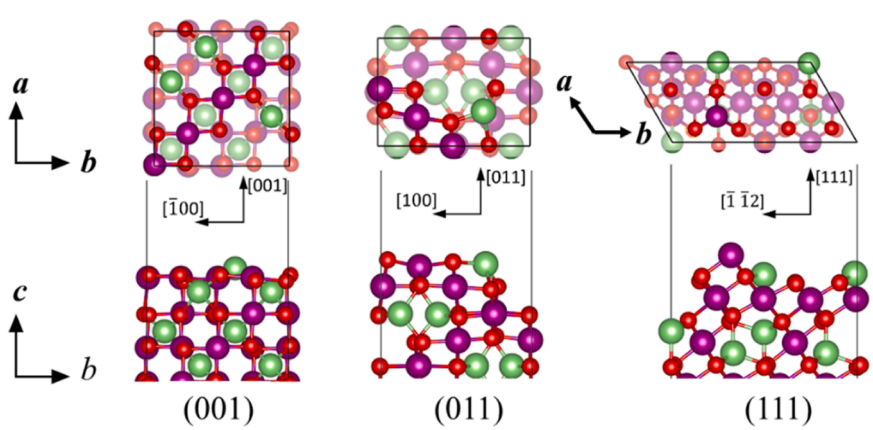

Fig. 2. (Top panels) top views and (bottom panels) side views of the (001), (011) and (111) surfaces of $LiMn_2O_4$. Li is green, Mn is violet, and O is red.

accompanied by minor contributions from *p* and *s* orbitals of Mn, O, and Li atoms, respectively. Furthermore, the calculated average atomic charges amount to 0.88, 1.78 and −1.10 e^-/atom for lithium, manganese, and oxygen, respectively. Collectively, the discussed bulk properties we in good agreement with experimental and available computation works noted.

3.2. Pristine surfaces

We employed the same models of the non-polar, stoichiometric, and symmetric low-Miller index surfaces of the $LiMn_2O_4$ material that we studied previously [79]. To facilitate the accommodation of the α-Al_2O_3 coating layers on these surfaces, while avoiding interactions among vertical periodic images, we introduced a vacuum region of 20 Å perpendicular to the slabs. Considering the high symmetry nature of a cubic system, several low Miller index surfaces are equivalent, for example {001} = (100), (010), and (001), whereas {011} = (110), (101), (011). Thus, we have considered only three low Miller index surfaces, *i.e.* the (001), (011) and (111) surfaces. For each of the simulated (001), (011) and (111) surfaces, we considered eight formula units (f.u.) with corresponding unit cell areas of 69.79, 49.28 and 60.40 Å^2, respectively. The four bottom-most atom layers were held fixed at their relaxed bulk positions, while the uppermost atom layers were permitted to relax unconstrainedly during the geometry optimizations.

The surface energies before (γ^{un}) and after (γ^{rel}) relaxation, were calculated using:

$$\gamma^{un} = \frac{E^{DFT}_{un,slab} - E^{DFT}_{bulk}}{2A_{slab}} \quad (1)$$

$$\gamma^{rel} = \frac{E^{DFT}_{rel,\ slab} - E^{DFT}_{bulk}}{A_{slab}} - \gamma^{un} \quad (2)$$

where E^{DFT}_{bulk}, $E^{DFT}_{un,\ slab}$, and $E^{DFT}_{rel,\ slab}$ denote the total energies of the optimized bulk, unrelaxed surface fixed at the optimized bulk positions, and half-relaxed surfaces, respectively, while *A* corresponds to their surface area. Their respective relaxation (*R*) percentages were calculated as:

$$R = \frac{\gamma^{un} - \gamma^{rel}}{\gamma^{un}} \times 100 \quad (3)$$

As was discussed previously [87], Table 1 summarizes the surface energy and relaxation percentages of the major $LiMn_2O_4$ surfaces, together with their respective average atomic charges (*q*), and work functions (ϕ). The work function (ϕ) was calculated as the difference between the electrostatic potential energy in the vacuum (E_{vac}) and the Fermi level of the material (E_F):

$$\phi = E_{vac} - E_F \quad (4)$$

The Li-terminated (001) surface has the lowest computed surface energy, recorded at $\gamma^{rel} = 0.037$ eV/Å^2, which is consistent with previously reported data [77,88,89]. Our calculations indicate that the (011) surface undergoes the largest relaxation percentage $R = 50.0$ % relative to the unrelaxed surface slab. The calculated average atomic charges observed for these stable terminations are comparable to the charges calculated for the bulk $LiMn_2O_4$ material [86], with the largest difference of ~2.6 % observed for the Mn atoms in the Li-terminated (001) surface. We also obtained the work function (ϕ) for each surface, which is the energy needed to extract an electron from the solid into the vacuum and was calculated as the difference between the electrostatic potential energy of the vacuum (E_{vac}) and the Fermi energy (E_F). Our calculated values for the work function suggest that the (011) surface exhibits lower reactivity compared to the (001) and (111) surfaces, whereas the (111) surface is predicted to be the most reactive.

Table 1
Surface energies before (γ^{un}) and after relaxation (γ^{rel}), percentage of relaxation (*R*) and work functions (ϕ) for the low-Miller index surfaces of $LiMn_2O_4$. The average charge (*q*) of the exposed atoms is also reported [79].

Properties	Surfaces		
	(001)	(011)	(111)
γ^{un} (eV/Å^2)	0.066	0.100	0.085
γ^{rel} (eV/Å^2)	0.037	0.050	0.052
R (%)	43.7	50.0	38.0
q(Li) (e^-/atom)	0.90	0.90	0.89
q(Mn) (e^-/atom)	1.73	1.74	1.74
q(O) (e^-/atom)	−1.09	−1.09	−1.10
ϕ(eV)	4.21	4.26	3.66

We have also modelled the seven low-Miller index surfaces of corundum α-Al_2O_3. Fig. 3 shows the optimized surface structures of the most stable terminations of α-Al_2O_3, whereas Table 2 lists their calculated surface energies before and after relaxation, relaxation percentage, average atomic charges, and work function. As discussed in our previous work [54], we calculated the lowest surface energy of $\gamma^{rel} = 0.11$ eV/Å^2 for the Al-terminated (0001), which is predicted to be the most stable surface under vacuum conditions, in agreement with earlier studies [90–92]. The second most stable surface is the O-terminated $(11\bar{2}0)$ facet with a surface energy of $\gamma^{rel} = 0.15$ eV/Å^2. The overall order of increasing surface energies of the alumina surfaces is (0001) < $(11\bar{2}0)$ < $(01\bar{1}0)$ < $(11\bar{2}1)$ < $(10\bar{1}1)$ < $(01\bar{1}1)$ < $(10\bar{1}0)$.

According to the calculated percentages of relaxation, the uppermost layers underwent significant adjustment during the optimization of all surfaces to their most stable configurations. The Al-terminated (0001) surface displays the largest relaxation percentage at 56.9 %, primarily attributed to the inward relaxation of dangling bonds along the *z*-direction. We also calculated the Bader charges for each atom on the surfaces, indicating a slight reduction compared to the values found for their fully coordinated counterparts in the bulk. For instance, we obtained an average charge depletion of *q*(Al) = 2.45 e^-/atom and an accumulation of *q*(O) = −1.63 e^-/atom for the (0001) surface, *i.e.* a difference of 1.22 % compared to the bulk. The calculated work functions (ϕ) reveal that the $(01\bar{1}1)$ surface is more reactive than the most stable (0001) surface by 0.22 eV.

Next, we constructed the particle morphologies of both materials using the surface energies of their respective low-Miller index surfaces. According to Wulff's theorem [93], the crystal in equilibrium has the height of the facet (h_i) directly proportional to its specific surface free energy (σ_i, where *i* = Miller index of the specific surface) and the ratio of the two is constant, which can be summarized by the expression:

$$\frac{\sigma_{(001)}}{h_{(001)}} = \frac{\sigma_{(011)}}{h_{(011)}} = \ldots = \frac{\sigma_i}{h_i} \quad (5)$$

The Wulff morphology of $LiMn_2O_4$ portrays a cuboctahedral particle with the (001) as the dominant plane, see Fig. 4a. This morphology also highlights a decreasing stability trend of (001) > (011) > (111). Upon delithiation, we observed that the (111) plane gained prominence whereas the (011) surface lost significance within the morphology [87]. As a result, our focus now centres on modelling the α-Al_2O_3-coated $LiMn_2O_4$ (001) and (111) surfaces. We obtained a hexagonal-prism shape for α-Al_2O_3 with a dominant Al-terminated (0001) plane and appearance of the $(11\bar{2}0)$ and $(01\bar{1}0)$ surfaces in smaller proportion. The other low-Miller index surfaces are not expressed due to their large surface energies with respect to the dominant (0001) surface, See Fig. 4b.

3.3. Heteroepitaxial interface

3.3.1. Geometrical misfit

Using the relaxed surfaces of the two materials that are prominent in the Wulff crystal morphology, we next investigated the deposition of α-Al_2O_3 onto the major $LiMn_2O_4$ (001) and (111) surfaces. Considering the incommensurate relationship of the surface lattices between the two

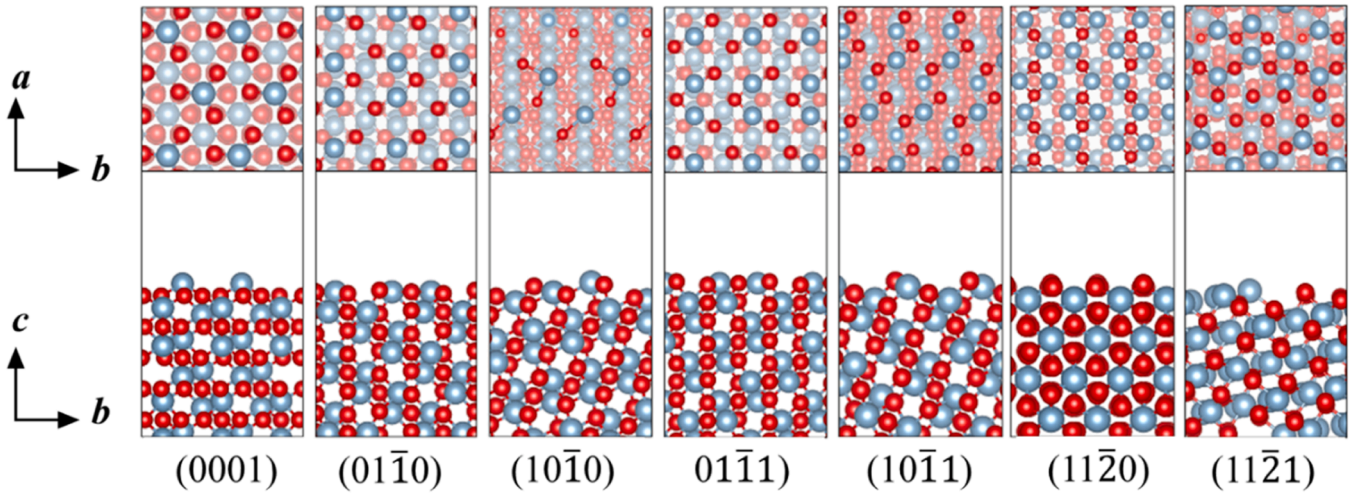

Fig. 3. (Top panels) top views and (bottom panels) side views of the seven low-Miller index surfaces of the α-Al_2O_3. Al is in blue, and O is in red.

Table 2
Calculated surface energies before (γ^{un}) and after relaxation (γ^{rel}), the percentage of relaxation (R) and work function for the seven α-Al_2O_3 low Miller index surfaces. The average charge (q) of the exposed atoms is also reported.

Property	Surfaces						
	(0001) [54]	(10$\bar{1}$0)	(01$\bar{1}$0)	(01$\bar{1}$1)	(10$\bar{1}$1)	(11$\bar{2}$0)	(11$\bar{2}$1)
γ^{un} (eV/Å^2)	0.25	3.96	0.24	1.99	1.98	0.19	0.30
γ^{rel} (eV/Å^2)	0.11	3.88	0.16	1.95	1.94	0.15	0.23
R (%)	56.9	2.0	33.4	2.3	1.9	22.3	24.8
q(Al) (e/atom)	2.45	2.34	2.43	2.37	2.47	2.46	2.35
q(O) (e/atom)	−1.63	−1.52	−1.61	−1.55	−1.65	−1.64	−1.57
ϕ(eV)	4.30	5.45	4.52	4.25	5.43	5.60	5.92

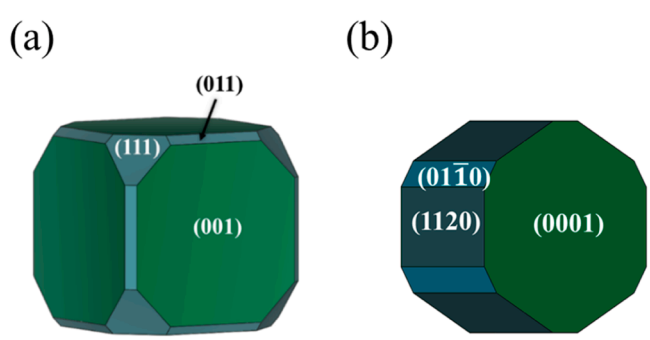

Fig. 4. Constructed Wulff morphologies of the pristine (a) $LiMn_2O_4$ and (b)α-Al_2O_3 surfaces.

materials, we first explored various potential configurations of the α-Al_2O_3 overlayer on the $LiMn_2O_4$ substrate surfaces to achieve optimal surface-to-surface alignment. To generate these configurations, we expanded the unit lattices of both the substrate and overlayer along the ***a*** and ***b*** directions using integers, as illustrated in Fig. 5a–b. The integers used to expand the spinel $LiMn_2O_4$ lattice in the ***a*** and ***b*** directions are denoted as k and l, while m and n represent the corresponding expansion factors for the α-Al_2O_3 overlayer surfaces. To assess the alignment of the surfaces, we employed the misfit (μ) calculation method introduced by Carter et al. [94–97]:

$$\mu = \left(1 - \frac{2\Omega}{A_{LMO} + A_{Al_2O_3}}\right) \times 100 \tag{6}$$

where A_{LMO} and $A_{Al_2O_3}$ are the surface areas of the $LiMn_2O_4$ substrate and α-Al_2O_3 overlayer in each interface and Ω is the overlap area between the surfaces of the two materials, see Fig. 5e-f. Since low misfit and lattice strain values can always be achieved at extremely large interface areas, which are, however, prohibitively costly for our DFT calculations, we have limited our interface lattice area to 450 Å^2.

Furthermore, since our simulations require boundary conditions, we imposed a degree of interfacial coherence, by adjusting the α-Al_2O_3 overlayer to accommodate the mismatch. We quantified this enforced strain on the overlayer with the variables δ_1^{nl} and δ_2^{km} calculated as:

$$\delta_1^{nl} = \frac{la_1 - nb_1}{nb_1} \tag{7}$$

$$\delta_2^{km} = \frac{ka_2 - mb_2}{mb_2} \tag{8}$$

where a_1 and a_2 denote the lengths of the basis vectors spanning the unit cell of the α-Al_2O_3 overlayer while b_1 and b_2 correspond to the unit cell of the $LiMn_2O_4$ substrate.

Experimentally, the feasibility of forming an epitaxial interface between the α-Al_2O_3 (0001) and $LiMn_2O_4$ (111) surfaces has been discussed [98,99]. However, understanding of the compatibility between the α-Al_2O_3 and $LiMn_2O_4$ (001) surfaces is limited. Fig. SI 1 illustrates all the possible configurations considered for the α-Al_2O_3 (0001)//$LiMn_2O_4$(111) interface, with Table 3 showing the misfit percentages relative to the matching area for the four systems with the lowest misfits. The lowest calculated misfit percentage was 2.75 % for the interface with the configuration $klmn$ = {1132}. The calculated strain of $\delta_1^{nl} = \delta_2^{km} = -0.57$ suggests that the α-Al_2O_3 overlayer should be compressed along both a and b to accommodate itself to the (111) surface of the substrate. To validate our findings, we also employed the near coincidence site lattice (NCSL) theory method proposed by Sayle et al. [100,101]. The same {1132} interface configuration was identified as having the lowest misfit, with negative strain values indicating

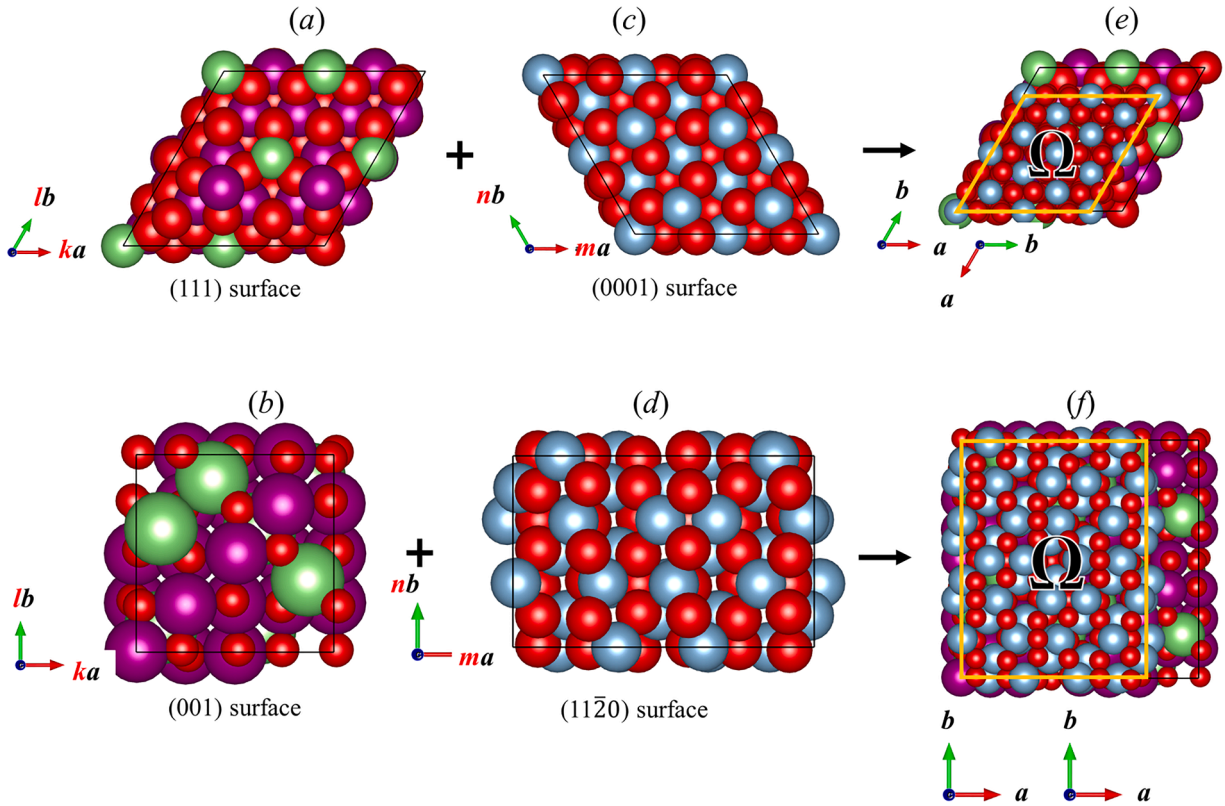

Fig. 5. Top views of the unit cells of the isolated (a) and (b) $LiMn_2O_4$ substrate and (c) and (d) α-Al_2O_3 overlayer surfaces. Both surfaces are supercells of a surface unit cell expanded along the *a* and *b* directions by the *k, l, m, n* integers shown in red. The overlap area (Ω) of both (e) α-Al_2O_3 (0001)// $LiMn_2O_4$ (111) and (f) α-Al_2O_3 (11$\bar{2}$0)//$LiMn_2O_4$ (001) interfaces before coherence is outlined in orange.

Table 3
Geometry misfit percentages (μ) and strain parameters (δ_1^{nl},δ_2^{km}) for various configurations of α-Al_2O_3 (0001) and (11$\bar{2}$0) surfaces on the major (001) and (111) surfaces of $LiMn_2O_4$.

Interface α-Al_2O_3//$LiMn_2O_4$	$LiMn_2O_4$		α-Al_2O_3		δ_1^{nl}	δ_2^{km}	Area (Å^2)	μ (%)
	k	*l*	*m*	*n*				
(0001)//(111)	1	1	3	2	−0.59	−0.59	112.81	2.75
	1	1	3	3	−0.73	−0.73	120.76	16.14
	1	1	2	2	−0.38	−0.38	79.03	17.91
	2	1	3	3	−0.45	−0.45	146.54	27.14
(11$\bar{2}$0)//(001)	3	1	2	1	−0.04	0.51	206.88	2.40
	2	1	1	1	0.28	1.02	107.75	12.65
	1	1	1	1	−0.36	0.01	68.96	22.18
	3	1	1	1	0.92	2.02	107.75	31.84

compression of the overlayer to accommodate the mismatch. A similar trend was observed for the second lowest misfit percentage, belonging to the {1133} configuration, see Table SI 2.

Consequently, our purpose was also to model the α-Al_2O_3 (0001)// $LiMn_2O_4$(111) interface and identify the α-Al_2O_3 surface that best aligns with the substrate (001) surface. To this end, we compared the lattices of the seven low-Miller indices surfaces of α-Al_2O_3 with the lattice of the $LiMn_2O_4$ (001) surface in order to identify an overlayer surface that fits with minimal strain. Three potential surfaces were examined further, *i.e.* the α-Al_2O_3 (10$\bar{1}$0), (01$\bar{1}$0) and (11$\bar{2}$0) facets. We then compared the misfit percentages of the α-Al_2O_3 (10$\bar{1}$0), (01$\bar{1}$0) and (11$\bar{2}$0) surfaces on the substrate $LiMn_2O_4$ (001) surface (see Figure SI 2). The lowest misfit percentage of 2.40 % indicates that the (11$\bar{2}$0) surface fits onto the (001) substrate surface with the geometry configuration *klmn* = {3121}. The calculated strain variables $\delta_1^{nl} = -0.04$ and $\delta_2^{km} = 0.51$ suggest that the (11$\bar{2}$0) surface should be compressed and expanded along *a* and *b*, respectively, to achieve coherence between the two materials. Given that interfaces with lattice mismatches exceeding 5 % are unlikely to exist, we have considered only geometry configurations with μ below that value.

3.3.2. Adhesion energies

To gain insight into the interfacial stability, we have computed the adhesion energy (E_{adh}), which measures the energy gained upon formation of the interface boundary between the two materials, as:

$$E_{adh} = \frac{(E_{Al_2O_3} + E_{LMO}) - E_{Inter}}{A} \quad (9)$$

where $E_{Al_2O_3}$ andE_{LMO} represent the total energies of an unsupported α-Al_2O_3 overlayer and a relaxed major surface of the $LiMn_2O_4$ substrate. The term E_{Inter} stands for the total energy of the relaxed heteroepitaxial interface while *A* denotes the interface area. Taking into consideration the influence of coating thickness on Li^+ intercalation during cycling [60], we examined heterostructures with various α-Al_2O_3 thicknesses (*i.e.* n_1, n_2, and n_3). All interfaces underwent adjustments to achieve the most stable configurations during relaxation. Fig. 6 summarizes the interfaces with different overlayer thicknesses and their corresponding adhesion energies. Positive values of interfacial energies signify stability, whereas negative values denote unstable heterostructures with respect to the free surfaces. Notably, the highest calculated energies were observed for the monolayer α-Al_2O_3 (n_1), with the most stable {1132} configuration yielding E_{adh} = 0.16 eV/Å. As the overlayer thickness is increased, E_{adh} decreases, suggesting that greater thickness leads to destabilization of the system. In contrast to experiments [57, 102,103] with amorphous coating thicknesses of up to 15 nm on an ~500 nm $LiMn_2O_4$ substrate, our computational method was unable to model such large systems due to the prohibitive computational cost of our DFT method for a large number of atoms. Our calculations also

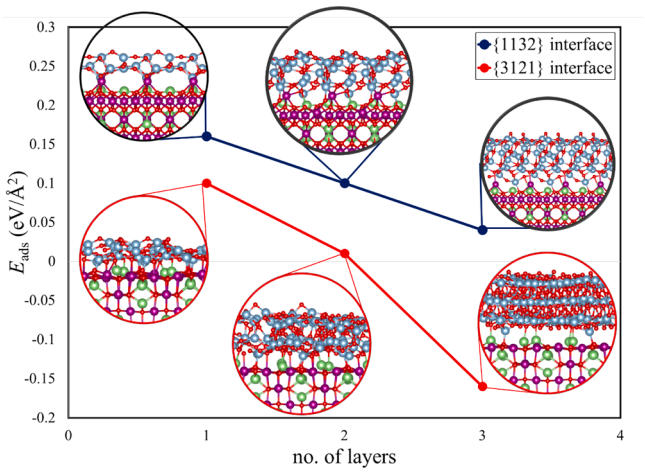

Fig. 6. Calculated adhesion energies for potential interfaces α-Al_2O_3 (0001)// $LiMn_2O_4$ (111) and α-$Al_2O_3(11\bar{2}0)$//$LiMn_2O_4$(001) with geometry configurations {1132} and {3121}, respectively, for various overlayer thicknesses.

revealed that overlayer-surface interactions at the boundary form Al-O, Mn-O and Li-O bonds, while subsequent α-Al_2O_3 overlayers exhibit disorder, except for the more crystalline n_3{3121} configuration.

3.3.3. Interplanar distances

We also investigated the interplanar distances (Δ_{ij}) of both the substrate and coating layers within the α-Al_2O_3 (0001)// $LiMn_2O_4$ (111) and α-$Al_2O_3(11\bar{2}0)$//$LiMn_2O_4$(001) interfaces with respect to their equivalent distances in the relaxed pristine surfaces (see Fig. 7). The interplanar distances of the α-Al_2O_3 and $LiMn_2O_4$ surfaces in the interfaces formed with varying number of coating layers were calculated as $\Delta_{ij} = \left(\frac{d_{ij}-d_{ij}^0}{d_{ij}^0}\right) \times 100$, where d_{ij} represents the separation distance between the relaxed i and $j = i + 1$ layers, and d_{ij}^0 is the corresponding distance in the pristine $LiMn_2O_4$ surfaces or the unsupported α-Al_2O_3 overlayer. As shown in Fig. 7 (a–b), it was evident that the atoms with dangling bonds of the (001) and (111) substrates were slightly displaced outward towards the interacting atoms of α-Al_2O_3 upon interface relaxation. The Mn atoms with dangling bonds in configuration {1132} moved outward in response to the formation of Mn-O and Al-O bonds with the α-Al_2O_3 coating, with the maximum shift of 3.8 % observed for n_3. Similarly, on the Mn-terminated (111) surface, the dangling bonds in the first atomic layer of the interface with configuration {3121} exhibited significant outward relaxation of 3.8 % for both n_3 and n_2. In both cases, the subsequent (MnO) layer experienced inward shifts of 1.1 and 1.9 % for n_1{1132} and n_3{3121}, respectively, during relaxation. Additionally, we noted minor relaxation in the subsequent layers of both interface models as we moved towards the lower planes where the atoms were fixed at their bulk positions.

Similarly, as shown in Fig. 7 (c–d), we analysed the shifts of the interplanar distances of the overlayer within the {3121} heterostructures in relation to the pristine unsupported α-Al_2O_3 surfaces. Our results show that the Al and O atoms are displaced inwards and

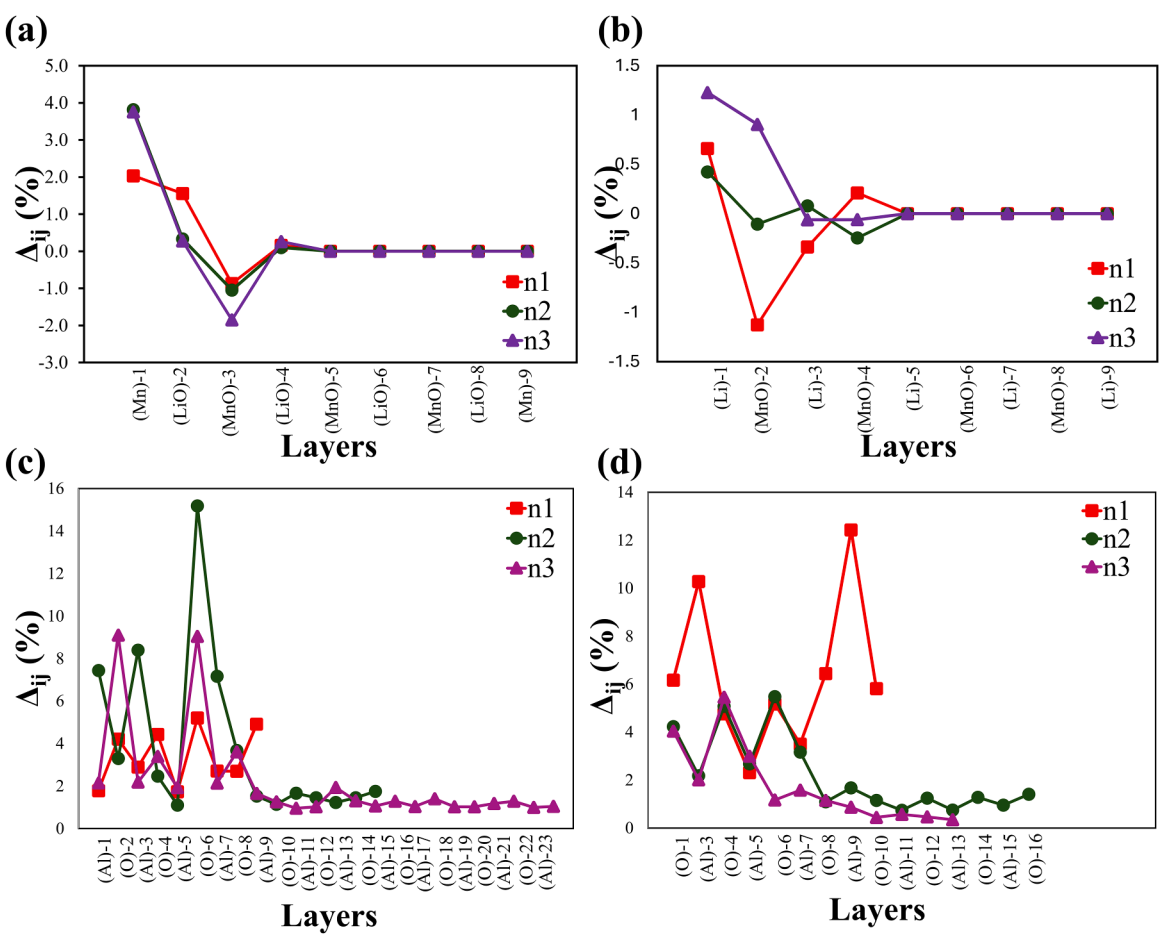

Fig. 7. Interplanar distance relaxation (Δ_{ij}) of the (a-b) $LiMn_2O_4$ (001) and (111) substrate surfaces and (c-d) α-Al_2O_3 (0001) and $(11\bar{2}0)$ overlayer surfaces in heterostructures compared to their isolated pristine counterparts for α-Al_2O_3(0001)//$LiMn_2O_4$(111) and α-$Al_2O_3(11\bar{2}0)$//$LiMn_2O_4$(001) with the configurations {1132} and {3121}, respectively, for various overlayer thicknesses.

outwards, respectively, upon formation of the Al-O and Mn-O interfacial bonds. However, a different trend was observed for the $1132n_2$ interface, where the Al ions moved outwards, suggesting a steric repulsion between the Mn/Li and Al atoms. The largest displacements were observed at 15.2 and 12.4 % for $1132n_2$ (O)−6 and $3121n_1$ (Al)−9, respectively, due to the formation of Al-O interfacial bonds. As the thickness of the coating layers was increased, we observed smaller interplanar relaxation, showing that the system tends to remain crystalline.

3.4. Electronic properties

We next quantified the electron charge accumulation/depletion of the $LiMn_2O_4$ substrate within the interface and compared it to the pristine surface, see Table 4. In general, we observed a minor gain in electronic charge on the substrate, which was provided by the α-Al_2O_3 overlayer in bothα-Al_2O_3(0001)//$LiMn_2O_4$(111) and α-Al_2O_3(11$\bar{2}$0)//$LiMn_2O_4$(001) hetero-structures with varying α-Al_2O_3 layers. The largest charge difference of $\Delta q = -0.90\ e^-$ was noted for the {3121} configuration with a single α-Al_2O_3 layer. However, a slight charge depletion of 0.06 e^- in the overlayer was observed for n_3{3121}, attributed to the formation of Al-O and Li-O bonds, which contributed −0.28 and −0.002 e^-, respectively. With the increase in the number of α-Al_2O_3 layers, the charge transfer tended to decrease except for n_2{1132}, which exhibited $\Delta q = -0.71\ e^-$. We further analysed the average charge transfer on the exposed Mn, Li, and O atoms of $LiMn_2O_4$ interacting with the overlayer and forming the Al-O, Mn-O and Li-O bonds. A consistent trend emerged of charge depletion from the interacting Mn atom to the overlayer O atom, reaching a maximum of 0.41 e^-/atom for n_2{1132}. As for the interacting Li atoms in the top layer, we observed a negligible charge accumulation from the overlayer O atom, with a minimal charge gain of $\Delta q = -0.002\ e^-$/atom. Similarly, a general charge accumulation was observed on the interacting oxygen in the top layer forming the Al-O bond, with a negligible charge gain of $\Delta q = -0.01\ e^-$/atom observed in the case of n_1{1132}. Notably, the charge transfer for Al-O interactions increased with the number of α-Al_2O_3 layers for {1132}, while the opposite trend was observed for {3121}.

Fig. 8 provides a visual representation of the charge density difference ($\Delta\rho$) between the two materials within the heterostructures. The $\Delta\rho$ values are depicted as the charge difference between the total charge density of the interfaces (ρ_{int}) and the sum of the electronic charge densities of the isolated $LiMn_2O_4$ and α-Al_2O_3 surfaces in the same geometry of the heterojunction, *i.e.* $\Delta\rho = \rho_{inter} - (\rho_{LMO} + \rho_{\alpha-Al_2O_3})$. These visualizations were generated using the VESTA (Visualization for Electronic and Structural Analysis) software [104], where yellow indicates charge accumulation and blue represents charge loss. Notably, the interaction involving Mn atoms exhibits charge depletion, which is offset by the accumulation of charge on the interacting O atoms within the α-Al_2O_3 overlayer. Additionally, we observed minor charge fluctuations on the neighbouring Al atom within the overlayer. The interacting O atom has a propensity for charge accumulation at the expense of the interacting Al atom. Conversely, minimal charge gain is observed along the Li-O bond, which is further observed on the neighbouring O atoms in the substrate $LiMn_2O_4$.

In conjunction with the charge transfer analysis, we also calculated the work function (ϕ), *i.e.* the energy required to remove an electron from the Fermi level into the vacuum. In both interface configurations, we noted the largest work function values for $n = 2$, with the peak value reaching 6.31 eV for the {3121} heterojunction. This trend of increasing work function values relative to the pristine surfaces implies that the coated surfaces become less reactive.

3.5. Partial delithiation thermodynamics

The mobility of lithium ions during cycling significantly impacts battery performance, affecting its capacity, energy density and cycle life. To gain insight into the effect of partial delithiation of the α-Al_2O_3-coated $LiMn_2O_4$ surfaces relative to the uncoated surfaces, we explored sequential Li removal from the top layers of the (001) and (111) surfaces of the spinel substrate within the α-Al_2O_3//$LiMn_2O_4$ interface, with varying α-Al_2O_3 thicknesses. The Li vacancy formation energies ($\Delta E^f_{inter-xLi}$) in the partially delithiated pristine/interface models were calculated and plotted against the number of Li atoms removed (see Fig. 9). For the pristine (001) and (111) surfaces, we consider the half-reaction at the cathode during cycling as follows:

$$LiMn_2O_4 \rightarrow Li_{1-x}Mn_2O_4 + xLi \tag{10}$$

In this process, lithium ions are extracted from the cathode and migrate through the electrolyte to the anode, while electrons traverse the external circuit to the anode, where Li atoms are formed. We simulated Li removal from the surfaces of the α-Al_2O_3//$LiMn_2O_4$ heterostructures as:

$$\text{Interface} \rightarrow \text{Interface}_{1-xLi} + xLi \tag{11}$$

The vacancy formation energies for the processes were calculated using:

$$\Delta E^f_{LMO-xLi} = (E_{LMO-xLi} + xE_{Li}) - E_{LMO} \tag{12}$$

$$\Delta E^f_{inter-xLi} = (E_{inter-xLi} + xE_{Li}) - E_{inter} \tag{13}$$

where $E_{LMO-xLi}$, $E_{inter-xLi}$ and E_{LMO}, E_{inter} are the total energies of the surfaces or interfaces with and without Li vacancies, while E_{Li} is the total energy of an isolated Li atom in a *bcc* unit cell and x is the number of lithium atoms removed. Positive values suggest that Li removal from the interfaces is an endothermic process, while an exothermic and favourable process would have a negative energy. Fig. 9 indicates that the removal of Li from the pristine $LiMn_2O_4$ material requires energy, as the calculated vacancy formation energies are all positive for both the (001) and (111) surfaces. This finding is in agreement with the operation principle of Li-ion batteries, since the charging process requires energy to move the Li^+ ions from the cathode to the anode material.

Relative to the pristine (001) and (111) surfaces of $LiMn_2O_4$, the lower vacancy formation energies in the α-Al_2O_3//$LiMn_2O_4$ heterostructures suggest that surface delithiation of the coated surfaces demands less energy. For the α-Al_2O_3(0001)//$LiMn_2O_4$(111) interface, the

Table 4
Electronic charge transfers on the $LiMn_2O_4$ substrate ($\Delta q(LiMn_2O_4)$) and individual interacting atoms (Δq(Li), Δq(Mn), and Δq(Al)). Positive charge transfer values indicate depletion while negative indicate accumulation. The work functions (ϕ) calculated for different numbers of α-Al_2O_3 layers are also reported.

Interface α-Al_2O_3//$LiMn_2O_4$	*klmn*	No. of layers	$\Delta q(LiMn_2O_4)$ (e^-)	Δq (e^-/atom)			ϕ (eV)
				q(Mn)	q(Al)	q(Li)	
(0001)//(111)	1132	n_1	−0.17	0.28	0.02	−0.023	5.78
		n_2	−0.71	0.83	−1.09	−0.015	5.87
		n_3	−0.08	0.28	−0.66	−0.004	5.39
(11$\bar{2}$0)//(001)	3121	n_1	−0.90	0.03	−0.25	−0.041	5.84
		n_2	−0.13	0.04	−0.26	0.019	6.31
		n_3	0.06	–	−0.28	−0.002	5.76

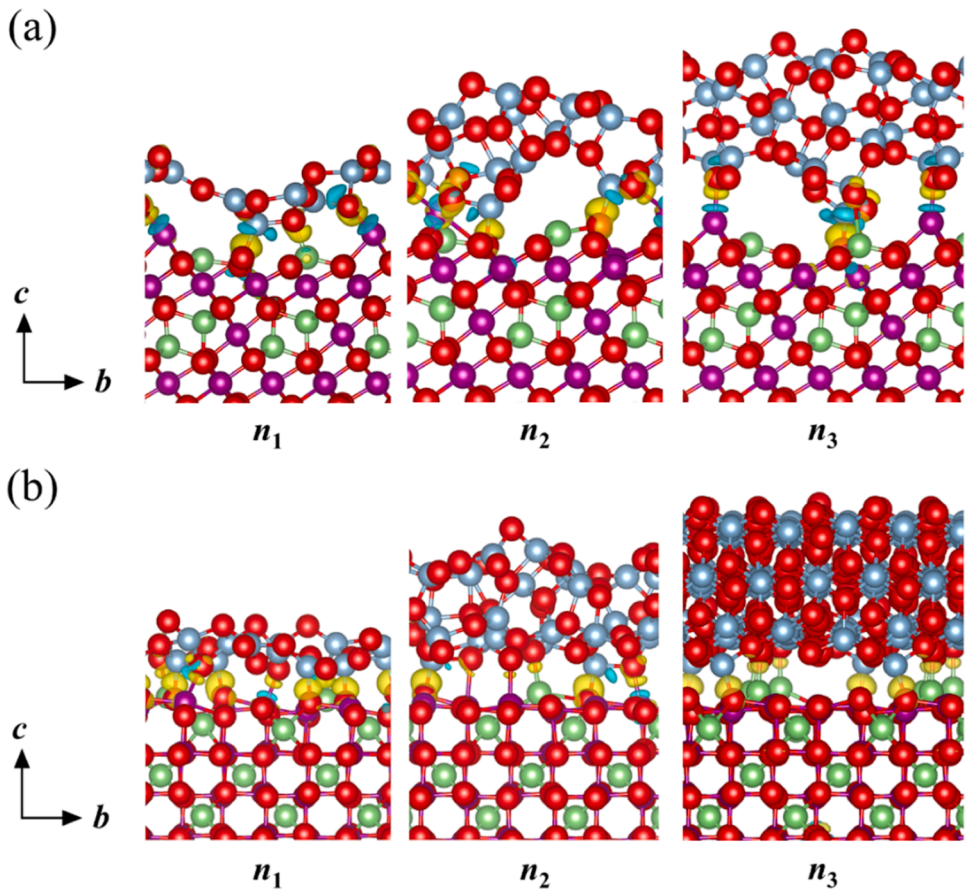

Fig. 8. Charge density difference (Δq) in the α-Al_2O_3//$LiMn_2O_4$ heterostructures with the (a) {1132} and (b) {3121} configurations and a varying number of overlayers (n_1, n_2, n_3). The isosurfaces are displayed at ± 0.0068, and ± 0.0076 e/Å^3, respectively. Accumulated charge is shown in yellow and charge depletion is indicated in blue.

monolayer (n_1) shows the lowest energy with n_2 and n_3 showing approximately the same energy for $x = 1$ and 2, but at $x = 3$, n_2 shows a relatively higher vacancy energy. At $x = 1$, the α-$Al_2O_3(11\bar{2}0)$// $LiMn_2O_4(001)$ interface containing a monolayer (n_1) and three layers (n_3) of α-Al_2O_3 with the {3121} configuration show the lowest vacancy formation energies of 2.16 and 1.89 eV, respectively. For the {3121} configuration, we found that n_3 has the lowest Li vacancy formation energy, although the monolayer n_1 becomes less endothermic with increased lithium removal.

Bader charge analysis of neighboring Mn atoms generally shows increased charge depletion, escalating as more Li vacancies are formed. Neighboring Mn atoms lose charge to the oxygen atoms compensating for the defects. The calculated work functions (ϕ) for the pristine surfaces rise with greater Li removal, signifying reducing their reactivity upon partial delithiation. Similar trends emerge for the heterostructures, with ϕ decreasing for the {1132} n_1 and n_2 configurations between $x = 1$ and 2, and for the {3121} n_1 configuration from $x = 0$ to 2, and slightly declining for n_2 between $x = 0$ and 1. However, compared to the pristine surfaces, lithium removal from the hetero-structures results in less reactive systems, except in the case of the{3121} n_1 configuration.

4. Conclusions

We have performed density functional theory (DFT+U) calculations to simulate the α-Al_2O_3//$LiMn_2O_4$ (001) and (111) interfaces to mimic the spinel $LiMn_2O_4$ cathode material coated with corundum α-Al_2O_3. We have followed the near coincidence site lattice (NCSL) theory method and determined that the {1132} and {3121} configurations provided the best alignment, with the lowest calculated misfit of 2.75 and 2.40 % for the α-$Al_2O_3(0001)$//$LiMn_2O_4(111)$ and α-$Al_2O_3(11\bar{2}0)$//$LiMn_2O_4(001)$ interfaces, respectively. The calculation of the adhesion energies for one (n_1), two (n_2) and three (n_3) α-Al_2O_3 overlayers suggest that the crystalline heterostructures become less stable as the coating thickness increases. The relaxation of the α-Al_2O_3 overlayer resulted in disorder at the boundaries for n_1, and n_2, but showed limited surface-surface changes at the boundaries for n_3. We observed minor electronic charge gain on the substrate, with negligible charge depletion in the overlayer α-Al_2O_3 for heterostructures at different coating thicknesses. Notably, the largest charge transfer of $\Delta q = -0.90\ e^-$ was calculated for n_1{3121}, which was because of the electronic density gains on the interacting O and Li atoms, forming Al-O and Li-O bonds, and partial depletion from the Mn atoms. For both interfaces, we observed the largest work function and smallest reactivity for $n = 2$.

Finally, we investigated the effect of Li vacancy formation to simulate the charged surfaces/interfaces. Our findings aligned with the theoretical understanding of Li-ion battery operation, as we observed an increase in vacancy formation energies corresponding to the number of Li atoms removed from both pristine $LiMn_2O_4$ (001) and (111) surfaces. This trend was consistent for the hetero-structures as well. Furthermore, our analysis of work functions suggested that the incorporation of an overlayer and partial delithiation led to a decrease in reactivity, except for n_1{3121}. These findings collectively contribute to our understanding of α-Al_2O_3 coatings and how they impact on the properties and behaviour of $LiMn_2O_4$ surfaces in the context of lithium-ion batteries.

In future work, we aim to explore the effects of temperature and the formation of an amorphous Al_2O_3 deposition using molecular dynamics techniques. In addition, we will aim to provide a clear understading of

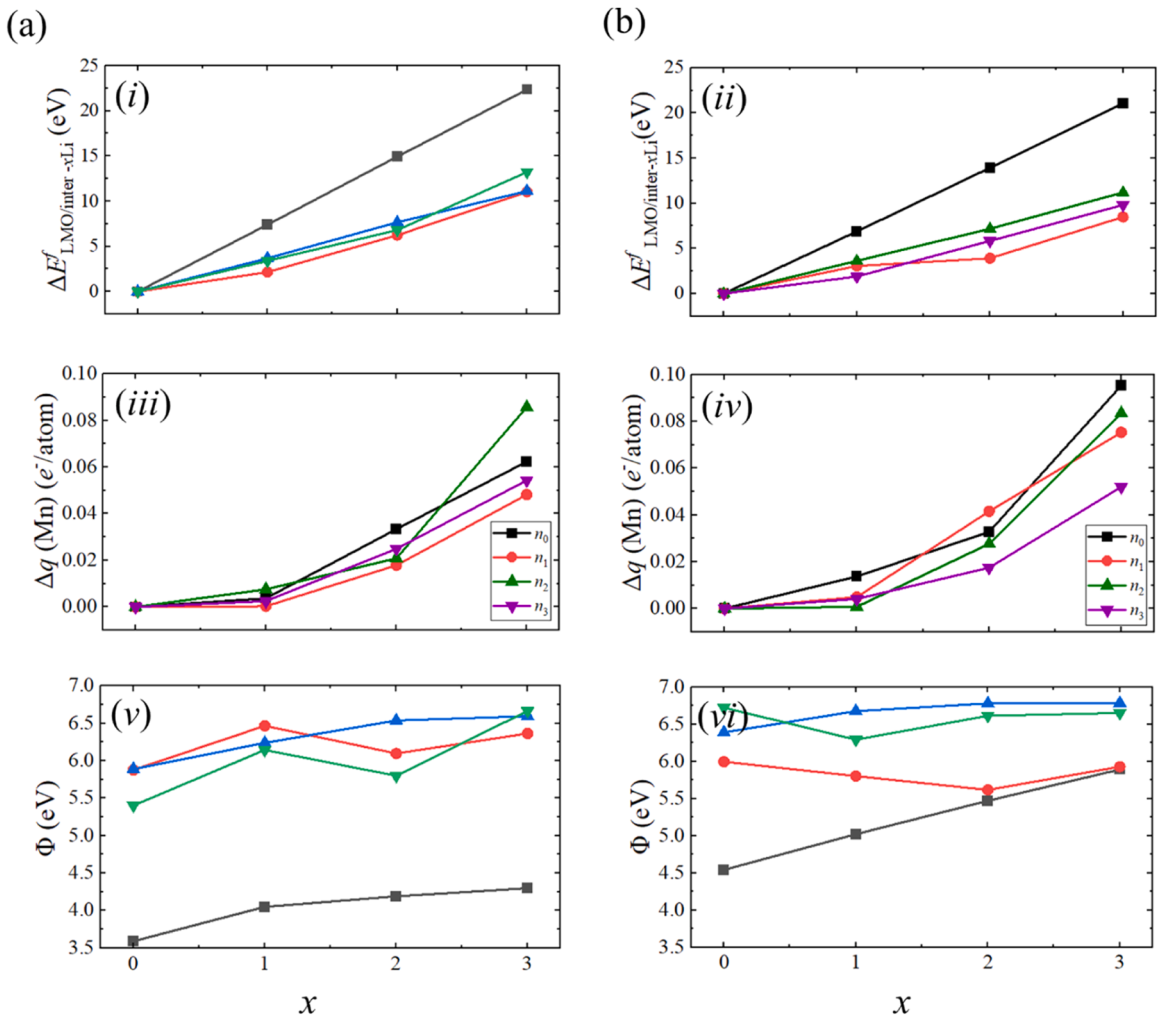

Fig. 9. Partial delithiation thermodynamic properties for (a) {1132} α-Al_2O_3(0001)//$LiMn_2O_4$(111) interface and (b) {3121} α-Al_2O_3(11$\bar{2}$0)//$LiMn_2O_4$(001) interface. The calculated properties include (*i* – *ii*) Li vacancy of formation ($\Delta E^f_{inter-xLi}$), (*iii* – *iv*) atomic Bader charges of Mn atoms near the vacancy (Δq (Mn)), and the (v – vi) work function (ϕ) as a function of number of lithium atoms removed (x).

the kinetics and themodynmic properties of the deposition of amorphous Al_2O_3 films and their effect on the electrolyte.

CRediT authorship contribution statement

Brian Ramogayana: Conceptualization, Investigation, Writing – original draft. **David Santos-Carballal:** Conceptualization, Project administration, Supervision, Validation, Writing – review & editing. **Khomotso P. Maenetja:** Supervision, Validation, Writing – review & editing. **Phuti E. Ngoepe:** Project administration, Supervision, Validation, Writing – review & editing. **Nora H. de Leeuw:** Project administration, Supervision, Validation, Writing – review & editing.

Declaration of competing interest

The authors declare that they have no known competing financial interests or personal relationships that could have appeared to influence the work reported in this paper.

Data availability

All data created during this research are provided in full in the results section of this paper and in the supplementary material.

Acknowledgements

The authors acknowledge funding from the UK Economic and Social Research Council (ESRC grant no. ES/N013867/1) and the National Research Foundation South Africa for facilitating the UK-SA Newton PhD partnership programme. PEN acknowledges the financial support of the DSI-NRF South African Research Chair Initiative and NHdL acknowledges the UK Engineering and Physical Sciences Research Council (EPSRC grant EP/K009567) for funding. We also appreciate the support received from the DSI Energy Storage Research Development and Innovation Initiative, South Africa. We acknowledge the use of the National Integrated Cyber Infrastructure System – CHPC, in Cape Town, South Africa, accessed through the Materials Modelling Centre (MMC), University of Limpopo. Via our membership of the UK's HEC Materials Chemistry Consortium, which is funded by EPSRC (EP/X035859), this work has used the ARCHER2 UK National Supercomputing Service (http://www.archer2.ac.uk). We acknowledge the support of the Supercomputing Wales project, which is part-funded by the European Regional Development Fund (ERDF) via the Welsh Government. Calculations were also undertaken on ARC4, part of the High-Performance Computing facilities at the University of Leeds, United Kingdom. For Open Access, the authors have applied a CC BY public copyright licence to any Author Accepted Manuscript version arising from this submission.

Supplementary materials

Supplementary material associated with this article can be found, in the online version, at doi:10.1016/j.surfin.2024.104316.

References

[1] M. Broussely, P. Biensan, B. Simon, Lithium insertion into host materials: the key to success for Li ion batteries, Electrochim. Acta 45 (1–2) (1999) 3–22.
[2] K. Nakahara, R. Nakajima, T. Matsushima, H. Majima, Preparation of particulate $Li_4Ti_5O_{12}$ having excellent characteristics as an electrode active material for power storage cells, J. Power Sources 117 (2003) 131.
[3] M. Hu, X. Pang, Z. Zhou, Recent progress in high-voltage lithium ion batteries, J. Power Sources 237 (2013) 229.
[4] M. Yuan, H. Liu, F. Ran, Fast-charging cathode materials for lithium & sodium ion batteries, Mater. Today 63 (2023) 360–379.
[5] K. Mizushima, P.C. Jones, P.J. Wiseman, J.B. Goodenough, $LixCoO_2$ ($0<x<-1$): a new cathode material for batteries of high energy density, Mater. Res. Bull. 15 (6) (1980) 783–789.
[6] N. Muralidharan, E.C. Self, M. Dixit, Z. Du, R. Essehli, R. Amin, J. Nanda, I. Belharouak, Next-generation cobalt-free cathodes–a prospective solution to the battery industry's cobalt problem, Adv. Energy Mater. (2022) 2103050.
[7] S. Saxena, C. Hendricks, M. Pecht, Cycle life testing and modeling of graphite/$LiCoO_2$ cells under different state of charge ranges, J. Power Sources 327 (2016) 394–400.
[8] J. Ying, C. Jiang, C. Wan, Preparation and characterization of high-density spherical $LiCoO_2$ cathode material for lithium ion batteries, J. Power Sources 129 (2) (2004) 264–269.
[9] S. Kalluri, M. Yoon, M. Jo, S. Park, S. Myeong, J. Kim, S.X. Dou, Z. Guo, J. Cho, Surface engineering strategies of layered $LiCoO_2$ cathode material to realize high-energy and high-voltage Li-Ion cells, Adv. Energy Mater. 7 (1) (2017) 1601507.
[10] J. Wang, N. Wang, W. Nan, C. Wang, X. Chen, X. Qi, S. Yan, S. Dai, Enhancement of electrochemical performance of $LiCoO_2$ cathode material at high cut-off voltage (4.5 V) by partial surface coating with graphene nanosheets, Int. J. Electrochem Sci. 15 (2020) 9282–9293.
[11] N.V. Kosova, N.F. Uvarov, E.T. Devyatkina, E.G. Avvakumov, Mechanochemical synthesis of $LiMn_2O_4$ cathode material for lithium batteries, Solid State Ion. 135 (1 – 4) (2000) 107–114.
[12] C.Y. Ouyang, S.Q. Shi, Z.X. Wang, H. Li, X.J. Huang, L.Q. Chen, Ab initio molecular-dynamics studies on $LixMn_2O_4$ as cathode material for lithium secondary batteries, Europhys. Lett. 67 (2004) 28.
[13] A.T. Phan, A.E. Gheribi, P. Chartrand, Modeling of coherent phase transformation and particle size effect in $LiFePO_4$ cathode material and application to the charging/discharging process, Electrochim. Acta 295 (2019) 632–644.
[14] C. Gong, Z. Xue, S. Wen, Y. Ye, X. Xie, Advanced carbon materials/olivine $LiFePO_4$ composites cathode for lithium ion batteries, J. Power Sources 318 (2016) 93–112.
[15] D.A. Cogswell, M.Z. Bazant, Size-dependent phase morphologies in $LiFePO_4$ battery particles, Electrochem. Commun. 95 (2018) 33–37.
[16] M.M. Thackeray, W.I.F. David, P.G. Bruce, J.B. Goodenough, Lithium insertion into manganese spinels, Mater. Res. Bull. 18 (4) (1983) 461–472.
[17] M.M. Thackeray, P.J. Johnson, L.A. De Picciotto, P.G. Bruce, J.B. Goodenough, Electrochemical extraction of lithium from $LiMn_2O_4$, Mater. Res. Bull. 19 (2) (1984) 179–187.
[18] J.C. Hunter, Preparation of a new crystal form of manganese dioxide: λ-MnO_2, J. Solid State Chem. 39 (2) (1981) 142–147.
[19] X. Li, Y. Xu, C. Wang, Suppression of Jahn–Teller distortion of spinel $LiMn_2O_4$ cathode, J. Alloys Compd. 479 (1 – 2) (2009) 310–313.
[20] B. Shibiri, R.S. Ledwaba, P.E. Ngoepe, Discharge induced structural variation of simulated bulk $Li_{1+x}Mn_2O_4$ ($0\leq x\leq 1$), Opt. Mater. (Amst.) 92 (2019) 67–70.
[21] D. Hlungwani, R.S. Ledwaba, P.E. Ngoepe, First-principles study on the effect of lithiation in spinel $Li_xMn_2O_4$ ($0\leq x\leq 1$) structure: calibration of CASTEP and ONETEP simulation codes, Materials (Basel) 15 (16) (2022) 5678.
[22] Y. Xia, Y. Zhou, M. Yoshio, Capacity fading on cycling of 4 V Li/$LiMn_2O_4$ cells, J. Electrochem. Soc. 144 (8) (1997) 2593.
[23] B.L. Rinkel, D.S. Hall, I. Temprano, C.P. Grey, Electrolyte oxidation pathways in lithium-ion batteries, J. Am. Chem. Soc. 142 (35) (2020) 15058–15074.
[24] J. Lu, K.S. Lee, Spinel cathodes for advanced lithium ion batteries: a review of challenges and recent progress, Mater. Technol. 31 (11) (2016) 628–641.
[25] C. Zhan, T. Wu, J. Lu, K. Amine, Dissolution, migration, and deposition of transition metal ions in Li-ion batteries exemplified by Mn-based cathodes–a critical review, Energy Environ. Sci. 11 (2) (2018) 243–257.
[26] Y. Tesfamhret, H. Liu, Z. Chai, E. Berg, R. Younesi, On the manganese dissolution process from $LiMn_2O_4$ cathode materials, ChemElectroChem 8 (8) (2021) 1516–1523.
[27] G. Xu, Z. Liu, C. Zhang, G. Cui, L. Chen, Strategies for improving the cyclability and thermo-stability of $LiMn_2O_4$-based batteries at elevated temperatures, J. Mater. Chem. A 3 (8) (2015) 4092–4123.
[28] A.H. Marincaş, P. Ilea, Enhancing lithium manganese oxide electrochemical behavior by doping and surface modifications, Coatings 11 (4) (2021) 456.
[29] Y. Huang, Y. Dong, S. Li, J. Lee, C. Wang, Z. Zhu, W. Xue, Y. Li, J. Li, Lithium manganese spinel cathodes for lithium-ion batteries, Adv. Energy Mater. 11 (2) (2021) 2000997.
[30] Y. Zhang, H. Xie, H. Jin, Q. Zhang, Y. Li, X. Li, K. Li, C. Bao, Research status of spinel $LiMn_2O_4$ cathode materials for Lithium ion batteries, IOP Confer. Ser.: Earth Environ. Sci. 603 (1) (2020) 012051.
[31] S. Zhang, W. Deng, R. Momen, S. Yin, J. Chen, A. Massoudi, G. Zou, H. Hou, W. Deng, X. Ji, Element substitution of a spinel $LiMn_2O_4$ cathode, J. Mater. Chem. A, 9(38) 9 (38) (2021) 21532–21550.
[32] Y. Xiao, X.D. Zhang, Y.F. Zhu, P.F. Wang, Y.X. Yin, X. Yang, J.L. Shi, J. Liu, H. Li, X.D. Guo, B.H. Zhong, Suppressing manganese dissolution via exposing stable {111} facets for high-performance Lithium-ion oxide cathode, Adv. Sci. 6 (13) (2019) 1801908.
[33] Y. Wu, C. Cao, J. Zhang, L. Wang, X. Ma, X. Xu, Hierarchical $LiMn_2O_4$ hollow cubes with exposed {111} planes as high-power cathodes for lithium-ion batteries, ACS Appl. Mater. Interfaces 8 (30) (2016) 19567–19572.
[34] F.P. Nkosi, C.J. Jafta, M. Kebede, L.Le Roux, M.K. Mathe, K.I. Ozoemena, Microwave-assisted optimization of the manganese redox states for enhanced capacity and capacity retention of $LiAl_xMn_{2-x}O_4$ (x= 0 and 0.3) spinel materials, RSC Adv. 5 (41) (2015) 32256–32262.
[35] C. Zhang, J. Su, Wang J, K. Yuan, C. Chen, S. Liu, T. Huang, J. Wu, H. Lu, A. Yu, Significant improvement on electrochemical performance of $LiMn_2O_4$ at elevated temperature by atomic layer deposition of TiO_2 nanocoating, ACS Sustain. Chem. Eng. 6 (6) (2018) 7890–7901.
[36] L.L. De Taeye, P.M. Vereecken, Chemo-mechanical effect of chlorine modified TiO_2 coatings on LMO, J. Mater. Chem. A 10 (2022) 24398–24409.
[37] B.H. Lee, B. Yoon, V.R. Anderson, S.M. George, Alucone alloys with tunable properties using alucone molecular layer deposition and Al_2O_3 atomic layer deposition, J. Phys. Chem. C 116 (5) (2012) 3250–3257.
[38] D. Kang, R.E. Warburton, A.U. Mane, J. Greeley, J.W. Elam, Modification of $LiMn_2O_4$ surfaces by controlling the Acid–Base surface chemistry of atomic layer deposition, Appl. Surf. Sci. 599 (2022) 153329.
[39] J. Tu, X.B. Zhao, J. Xie, G.S. Cao, D.G. Zhuang, T.J. Zhu, J.P. Tu, Enhanced low voltage cycling stability of $LiMn_2O_4$ cathode by ZnO coating for lithium ion batteries, J. Alloys Compd. 432 (2007) 313–317.
[40] X. Liu, J. Wang, J. Zhang, S. Yang, Sol–gel-template synthesis of ZnO nanotubes and its coaxial nanocomposites of $LiMn_2O_4$/ZnO, Mater. Sci. Eng. A 430 (2006) 248–253.
[41] S. Aziz, J. Zhao, C. Cain, Y. Wang, Nanoarchitectured $LiMn_2O_4$/Graphene/ZnO Composites as electrodes for Lithium ion batteries, J. Mater. Sci. Technol. 30 (5) (2014) 427–433.
[42] J.S. Gnanaraj, V.G. Pol, A. Gedanken, D. Aurbach, Improving the high-temperature performance of $LiMn_2O_4$ spinel electrodes by coating the active mass with MgO via a sonochemical method, Electrochem. Commun. 5 (2003) 940–945.
[43] S. Lim, J. Cho, PVP-functionalized nanometre scale metal oxide coatings for cathode materials: successful application to $LiMn_2O_4$ spinel nanoparticles, Chem. Commun. (2008) 4472–4474.
[44] A. Tron, Y.D. Park, J. Mun, AlF_3-coated $LiMn_2O_4$ as cathode material for aqueous rechargeable lithium battery with improved cycling stability, J. Power Sources 325 (2016) 360–364.
[45] K. Park, J.H. Park, S.G. Hong, J. Yoon, S. Park, J.H. Kim, D. Yoon, H. Kim, Y. H. Son, J.H. Park, S. Kwon, Induced AlF_3 segregation for the generation of reciprocal Al_2O_3 and LiF coating layer on self-generated $LiMn_2O_4$ surface of over-lithiated oxide based Li-ion battery, Electrochim. Acta 222 (2016) 830–837.
[46] J.G. Li, X.M. He, R.S. Zhao, Electrochemical performance of SrF_2-coated $LiMn_2O_4$ cathode material for Li-ion batteries, Trans. Nonferr. Metals Soc. Chin. 17 (6) (2007) 1324–1327.
[47] Q. Chena, Y. Wanga, T. Zhang, W. Yina, J. Yang, X. Wang, Electrochemical performance of LaF_3-coated $LiMn_2O_4$ cathode materials for lithium ion batteries, Electrochim. Acta 83 (2012) 65–72.
[48] R. He, A. Wei, X. Bai, L. Zhang, X. Li, J. Mu, X. Zhang, J. Ge, Z. Liu, Enhanced cycling performance of Li ion batteries based on Ni-rich cathode materials with $LaPO_4$/Li_3PO_4 co-modification, Ceram. Int. 47 (24) (2021) 34585–34594.
[49] P. Mohan, G.P. Kalaignan, Structure and electrochemical performance of surface modified $LaPO_4$ coated $LiMn_2O_4$ cathode materials for reachargeable lithium batteries, Ceram. Int. 40 (2014) 1415–1421.
[50] S. Zhoa, Y. Bai, L. Ding, B. Wang, W. Zhang, Enhanced cycling stability and thermal stability of YPO_4 -coated $LiMn_2O_4$ cathode materials for lithium ion batteries, Solid State Ion. 247 (248) (2013) 22–29.
[51] C. Qing, Y. Bai, J. Yang, W. Zhang, Enhanced cycling stability of $LiMn_2O_4$ cathode by amorphous $FePO_4$ coating, Electrochim. Acta 56 (2011) 6612–6618.
[52] F. Wu, X. Zhang, T. Zhao, L. Li, M. Xie, R. Chen, Multifunctional $AlPO_4$ coating for improving electrochemical properties of low-cost $Li[Li_{0.2}Fe_{0.1}Ni_{0.15}Mn_{0.55}]O_2$ cathode materials for lithium-ion batteries, ACS Appl. Mater. Interfaces 7 (6) (2015) 3773–3781.
[53] B.A. Vázquez, P. Pena, A.H. De Aza, M.A. Sainz, A. Caballero, Corrosion mechanism of polycrystalline corundum and calcium hexaluminate by calcium silicate slags, J. Eur. Ceram. Soc. 29 (8) (2009) 1347–1360.
[54] B. Ramogayana, D. Santos-Carballal, K.P. Maenetja, N.H. de Leeuw, P.E. Ngoepe, Density functional theory study of ethylene carbonate adsorption on the (0001) surface of aluminum oxide α-Al_2O_3, ACS Omega 6 (44) (2021) 29577–29587.
[55] S.T. Myung, K. Izumi, S. Komaba, Y.K. Sun, H. Yashiro, N. Kumagai, Role of alumina coating on Li− Ni− Co− Mn− O particles as positive electrode material for lithium-ion batteries, Chem. Mater. 17 (14) (2005) 3695–3704.
[56] A.M. Kannan, A. Manthiram, Surface/chemically modified $LiMn_2O_4$ cathodes for lithium-ion batteries, Electrochem. Solid-State Lett. 5 (7) (2002) A167.
[57] A. Eftekhari, Aluminum oxide as a multi-function agent for improving battery performance of $LiMn_2O_4$ cathode, Solid State Ion. 167 (3–4) (2004) 237–242.

[58] J. Tu, X.B. Zhao, G.S. Cao, D.G. Zhuang, T.J. Zhu, J.P. Tu, Enhanced cycling stability of $LiMn_2O_4$ by surface modification with melting impregnation method, Electrochim. Acta 51 (28) (2006) 6456–6462.
[59] C.Y. Ouyang, X.M. Zeng, Z. Sljivancanin, A. Baldereschi, Oxidation states of Mn atoms at clean and Al_2O_3-covered $LiMn_2O_4$ (001) surfaces, J. Phys. Chem. C 114 (10) (2010) 4756–4759.
[60] U. Nisar, N. Muralidharan, R. Essehli, R. Amin, I. Belharouak, Valuation of surface coatings in high-energy density lithium-ion battery cathode materials, Energy Storage Mater. 38 (2021) 309–328.
[61] D. Guan, J.A. Jeevarajan, Y. Wang, Enhanced cycleability of LiMn2O4 cathodes by atomic layer deposition of nanosized-thin Al_2O_3 coatings, Nanoscale 3 (4) (2011) 1465–1469.
[62] G.H. Waller, P.D. Brooke, B.H. Rainwater, S.Y. Lai, R. Hu, Y. Ding, F.M. Alamgir, K.H. Sandhage, M.L. Liu, Structure and surface chemistry of Al_2O_3 coated $LiMn_2O_4$ nanostructured electrodes with improved lifetime, J. Power Sources 306 (2016) 162–170.
[63] F. Lai, X. Zhang, H. Wang, S. Hu, X. Wu, Q. Wu, Y. Huang, Z. He, Q. Li, Three-dimension hierarchical Al_2O_3 nanosheets wrapped $LiMn_2O_4$ with enhanced cycling stability as cathode material for lithium ion batteries, ACS Appl. Mater. Interfaces 8 (33) (2016) 21656–21665.
[64] R.E. Warburton, M.J. Young, S. Letourneau, J.W. Elam, J. Greeley, Descriptor-based analysis of atomic layer deposition mechanisms on spinel $LiMn_2O_4$ lithium-ion battery cathodes, Chem. Mater. 32 (5) (2020) 1794–1806.
[65] M.J. Young, S. Letourneau, R.E. Warburton, W.M. Dose, C. Johnson, J. Greeley, J, J.W. Elam, High-rate spinel $LiMn_2O_4$ (LMO) following carbonate removal and formation of Li-rich interface by ALD treatment, J. Phys. Chem. C 123 (39) (2019) 23783–23790.
[66] L. Chen, R.E. Warburton, K.S. Chen, J.A. Libera, C. Johnson, Z. Yang, M. C. Hersam, J.P. Greeley, J.W. Elam, Mechanism for Al_2O_3 atomic layer deposition on $LiMn_2O_4$ from in situ measurements and ab initio calculations, Chem 4 (10) (2018) 2418.
[67] G. Kresse, J. Furthmüller, Efficient iterative schemes for ab initio total-energy calculations using a plane-wave basis set, Phys. Rev. B 54 (16) (1996) 11169.
[68] J.P. Perdew, K. Burke, M. Ernzerhof, Generalized gradient approximation made simple, Phys. Rev. Lett. 77 (18) (1996) 11169–11186.
[69] P.E. Blöchl, Projector augmented-wave method, Phys. Rev. B 50 (24) (1994) 17953–17979.
[70] G. Kresse, D. Joubert, From ultrasoft pseudopotentials to the projector augmented-wave method, Phys. Rev. B 19 (3) (1999) 1758–1775.
[71] S. Grimme, S. Ehrlich, L. Goerigk, Effect of the damping function in dispersion corrected density functional theory, J. Comput. Chem. 32 (7) (2011) 1456–1465.
[72] S. Grimme, J. Antony, S. Ehrlich, H. Krieg, A consistent and accurate ab initio parametrization of density functional dispersion correction (DFT-D) for the 94 elements H-Pu, J. Chem. Phys. 132 (15) (2010) 154104.
[73] P.E. Blöchl, O. Jepsen, O.K. Andersen, Improved tetrahedron method for Brillouin-zone integrations, Phys. Rev. B 49 (23) (1994) 16223–16233.
[74] V.I. Anisimov, M.A. Korotin, J. Zaanen, O.K. Andersen, Spin bags, polarons, and impurity potentials in $La_{2-x}Sr_xCuO_4$ from first principles, Phys. Rev. Lett. 68 (3) (1992) 345–348.
[75] S.L. Dudarev, G.A. Botton, S.Y. Savrasov, C.J. Humphreys, A.P. Sutton, Electron-energy-loss spectra and the structural stability of nickel oxide: an LSDA+ U study, Phys. Rev. B 57 (3) (1998) 1505–1509.
[76] J. Bhattacharya, C. Wolverton, Relative stability of normal vs. inverse spinel for 3d transition metal oxides as lithium intercalation cathodes, Phys. Chem. Chem. Phys. 15 (17) (2013) 6486–6498.
[77] A. Karim, S. Fosse, K.A. Persson, Surface structure and equilibrium particle shape of the $LiMn_2O_4$ spinel from first-principles calculations, Phys. Rev. B 87 (7) (2013) 075322–1-075322-6.
[78] K.T. Malatji, D. Santos-Carballal, U. Terranova, P.E. Ngoepe, N.H. de Leeuw, Controlling the lithium intercalation voltage in the $Li(Mn_{1-x}Ni_x)_2O_4$ spinel via tuning of the Ni concentration: a density functional theory study, South Afr. J. Chem. 74 (2021) 3–7.
[79] B. Ramogayana, D. Santos-Carballal, P.A. Aparicio, M.G. Quesne, K.P. Maenetja, P.E. Ngoepe, N.H. de Leeuw, Ethylene carbonate adsorption on the major surfaces of lithium manganese oxide $Li_{1-x}Mn_2O_4$ spinel ($0.000 < x < 0.375$): a DFT+U-D3 study, Phys. Chem. Chem. Phys. 22 (12) (2020) 6763–6771.
[80] J.L. Quan, B.T. Teng, X.D. Wen, Y. Zhao, R. Liu, M.F. Luo, Hydrogen fluoride adsorption and reaction on the α-Al_2O_3 (0001) surface: a density functional theory study, J. Chem. Phys. 136 (11) (2012) 114701.
[81] W.Y. Ching, Y.N. Xu, First-principles calculation of electronic, optical, and structural properties of α-Al_2O_3, J. Am. Ceram. Soc. 77 (2) (1994) 404–411.
[82] J.A. Spencer, A.L. Mock, A.G. Jacobs, M. Schubert, Y. Zhang, M.J. Tadjer, A review of band structure and material properties of transparent conducting and semiconducting oxides: Ga_2O_3, Al_2O_3, In_2O_3, ZnO, SnO_2, CdO, NiO, CuO, and $Sc2O_3$, Appl. Phys. Rev. 9 (1) (2022) 011315.
[83] S. Watanabe, T. Sasaki, R. Taniguchi, T. Ishii, K. Ogasawara, First-principles calculation of ground and excited-state absorption spectra of ruby and alexandrite considering lattice relaxation, Phys. Rev. B 79 (7) (2009) 075109.
[84] R. Bharthasaradhi, L.C. Nehru, Structural and phase transition of α-Al_2O_3 powders obtained by co-precipitation method, Phase Transit. 89 (1) (2016) 77–83.
[85] G. Rousse, C. Masquelier, J. Rodriguez-Carvajal, E. Elkaim, J.P. Lauriat, J. L. Martinez, X-ray study of the spinel $LiMn_2O_4$ at low temperatures, Chem. Mater. 11 (12) (1999) 3629–3635.
[86] D. Santos-Carballal, P.E. Ngoepe, N.H. de Leeuw, Ab initio investigation of the thermodynamics of cation distribution and of the electronic and magnetic structures in the $LiMn_2O_4$ spinel, Phys. Rev. B 97 (8) (2018) 085126–1-085126-11.
[87] B. Ramogayana, D. Santos-Carballal, K.P. Maenetja, K.T. Malatji, N.H. de Leeuw, P.E. Ngoepe, A DFT+ U-D3 study of the adsorption of hydrogen fluoride and ethylene carbonate on the niobium-doped (001), (011), and (111) surfaces of lithium manganese oxide, J. Electrochem. Soc. 169 (9) (2022) 090507.
[88] R.E. Warburton, H. Iddir, L.A. Curtiss, J. Greeley, Thermodynamic stability of low-and high-index spinel $LiMn_2O_4$ surface terminations, ACS Appl. Mater. Interfaces 8 (17) (2016) 11108–11121.
[89] M.M. Hasan, P.P. Dholabhai, R.H. Castro, B.P. Uberuaga, Stabilization of $MgAl_2O_4$ spinel surfaces via doping, Surf. Sci. 649 (2016) 138–145.
[90] N.H. de Leeuw, S.C. Parker, Effect of chemisorption and physisorption of water on the surface structure and stability of alpha-alumina, J. Am. Ceram. Soc. 82 (11) (1999), 3209-2316.
[91] S. Alavi, D.C. Sorescu, D.L. Thompson, Adsorption of HCl on single-crystal α-Al_2O_3 (0001) surface: a DFT study, J. Phys. Chem. B 107 (1) (2003) 186–195.
[92] C.E. Nelson, J.W. Elam, M.A. Tolbert, S.M. George, H_2O and HCl adsorption on single crystal α-Al_2O_3 (0001) at stratospheric temperatures, Appl. Surf. Sci. 171 (1–2) (2001) 21–33.
[93] G. Wulff, On the question of speed of growth and dissolution of crystal surfaces. 34(5/6), p.449, Z. Kristallogr. 34 (1901) 449–530.
[94] A. Christensen, E.A. Carter, First-principles characterization of a heteroceramic interface: ZrO_2 (001) deposited on an α- Al_2O_3 (11 0 2) substrate, Phys. Rev. B 62 (24) (2000) 16968.
[95] L.I. Bendavid, E.A. Carter, First principles study of bonding, adhesion, and electronic structure at the Cu_2O (111)/ZnO(1010) interface, Surf. Sci. 618 (2013) 62–71.
[96] O. Lupan, D. Santos-Carballal, N. Magariu, A.K. Mishra, N. Ababii, H. Krüger, N. Wolff, A. Vahl, M.T. Bodduluri, N. Kohlmann, L. Kienle, Al_2O_3/ZnO heterostructure-based sensors for volatile organic compounds in safety applications, ACS Appl. Mater. Interfaces 14 (25) (2022) 29331–29344.
[97] D. Santos-Carballal, O. Lupan, N. Magariu, N. Ababii, H. Krüger, M.T. Bodduluri, N.H. De Leeuw, S. Hansen, R. Adelung, Al_2O_3/ZnO composite-based sensors for battery safety applications: an experimental and theoretical investigation, Nano Energy 109 (2023) 108301.
[98] Y.H. Ikuhara, X. Gao, R. Huang, C.A. Fisher, A. Kuwabara, H. Moriwake, K. Kohama, Epitaxial growth of $LiMn_2O_4$ thin films by chemical solution deposition for multilayer lithium-ion batteries, J. Phys. Chem. C 118 (34) (2014) 19540–19547.
[99] Y.H. Ikuhara, X. Gao, K. Kawahara, C.A. Fisher, A. Kuwabara, R. Ishikawa, H. Moriwake, Y. Ikuhara, Atomic-level changes during electrochemical cycling of oriented $LiMn_2O_4$ cathodic thin films, ACS Appl. Mater. Interfaces 14 (5) (2022) 6507–6517.
[100] T.X.T. Sayle, C.R.A. Catlow, D.C. Sayle, S.C. Parker, J.H. Harding, Computer simulation of thin film heteroepitaxial ceramic interfaces using a near-coincidence-site lattice theory, Philos. Mag. A 68 (3) (1993) 565–573.
[101] D.C. Sayle, T.X.T. Sayle, S.C. Parker, J.H. Harding, C.R.A. Catlow, The stability of defects in the ceramic interfaces, MgO/MgO and CeO_2/Al_2O_3, Surf. Sci. 334 (1–3) (1995) 170–178.
[102] H. Liu, F. Yang, J. Guo, M. Xiang, H. Bai, R. Wang, C. Su, Facile combustion synthesis of amorphous Al_2O_3-coated $LiMn_2O_4$ cathode materials for high-performance Li-ion batteries, New J. Chem. 45 (23) (2021) 10534–10540.
[103] S. Li, K. Zhu, D. Zhao, Q. Zhao, N. Zhang, Porous $LiMn_2O_4$ with Al_2O_3 coating as high-performance positive materials, Ionics (Kiel) 25 (2019) 1991–1998.
[104] K. Momma, F. Izumi, VESTA 3 for three-dimensional visualization of crystal, volumetric and morphology data, J. Appl. Crystallogr. 44 (6) (2011) 1272–1276.